ASCE

Experimental Investigation of Friction at Buckling-Restrained Brace Debonding Interfaces

Ben Sitler, Dr.Eng., P.E., M.ASCE[1]; Toru Takeuchi, Dr.Eng., A.M.ASCE[2]; Yuki Terazawa, Dr.Eng.[3]; and Masao Terashima, Ph.D.[4]

Abstract: The friction behavior of mortar–polymer–steel debonding interfaces was experimentally investigated to support numerical simulation of buckling-restrained braces (BRBs). Characteristic contact and slip demands were developed using two-dimensional Abaqus models to inform a full-scale test program. A stabilized dynamic friction coefficient of 0.065 was observed for reciprocating *two-way* sliding at the reference bearing pressure (20 MPa), slip amplitude (±20 mm), and velocity (30 mm/s) but increased to 0.16 at low bearing pressures and reduced to 0.03 for quasi-static loading. A recurring 40% dynamic amplification was observed in each *one-way* sliding cycle, where contact was only applied in one direction of the reciprocating motion, replicating the actual condition of BRB wavecrests. A system wear effect was also observed where small patches of mortar were exposed and then resurfaced, increasing the smeared friction coefficient by up to 0.15. Finally, the compressible debonding gap closely matched the polymer thickness, excluding textile backing, if present. A nonlinear friction model dependent on pressure–velocity–distance was developed, and recommendations were made to improve common testing provisions.
DOI: 10.1061/(ASCE)ST.1943-541X.0003184.

Author keywords: Buckling-restrained brace; Friction; Debonding interface.

Introduction

Buckling-restrained braces (BRBs) are seismic devices composed of a tapered, energy-dissipating steel core encased in an axially decoupled restrainer, which is separated by a debonding interface. The debonding interface serves two purposes: to create a gap that accommodates compressive Poisson expansion of the yielded core and reduce friction at wavecrests that form as the core undergoes small-amplitude higher-mode buckling during compression half-cycles. These design objectives may be met using the debonding interfaces classified in Fig. 1. These include a thin antifriction material that undergoes plastic deformation with an internal slip plane (Interface type I), a thick antifriction material that compresses elastically and slides against the core plate (Interface type II), or a hard antifriction material that is offset by compressible filler or removable spacers and slides against the core plate (Interface type III). Bare steel–steel or steel–mortar interfaces with an air gap are also feasible (Interface type IV), but at the cost of a higher friction coefficient, while lubricants requiring maintenance are undesirable given that most applications have a multidecade design life and the BRB or interface is often inaccessible.

Selecting an appropriate type of debonding interface depends on the desired performance, restrainer composition, and fabrication method. In a typical construction of mortar-filled steel-tube BRBs, which are widely used in practice, the debonding material is first attached to the core plate before placing the core in the steel tube and casting the mortar, which imposes a small hydrostatic pressure on the order of 0.05–0.5 MPa and bonds to the debonding material. For this type of BRB, good performance has been achieved using a soft, thin film of butyl, chloroprene, or silicon rubber (Chen et al. 2016; Guo et al. 2017; Iwata et al. 2000; Tsai et al. 2014). However, despite extensive device-level testing (Black et al. 2004; Tsai et al. 2014), there are few to no direct friction data for these Interface type I materials under the unique sliding conditions experienced in BRBs.

The primary use case for the friction coefficient in BRBs is to numerically simulate the effects of higher-mode buckling of the core plate using nonlinear finite-element software, such as LS-Dyna, Abaqus, and Ansys. However, owing to a lack of direct friction data, current practice is to adopt a Coulomb friction model calibrated against peak BRB forces (Avci-Karatas et al. 2019; Budaházy and Dunai 2015; Chen et al. 2016; Guo et al. 2017; Stratan et al. 2020). These constant friction coefficients have varied from $\mu = 0.03$ to 0.5, but $\mu = 0.1$ is the most common estimate. Unfortunately, this trial-and-error procedure is potentially error prone because friction is a second-order force in BRBs and the friction coefficient may vary with the core geometry. Indirect calibration may mask compensating errors that affect key failure modes, and so a direct experimental basis for the friction coefficient is preferred.

Direct experimental data are particularly important for polymers [e.g., polytetrafluoroethylene (PTFE), ultra-high-molecular-weight polyethylene (UHMWPE), rubber], because the friction coefficient tends to decrease with pressure and temperature (ambient and cyclic heating) but increase with velocity (Stachowiak and Batchelor 2014). Adhesion results in significant material transfer to

[1]Dept. of Architecture, Tokyo Institute of Technology, 2-12-1 Ōokayama, Meguro-ku, Tokyo 152-8550, Japan (corresponding author). ORCID: https://orcid.org/0000-0001-5551-9879. Email: sitler.b.aa@m.titech.ac.jp

[2]Professor, Dept. of Architecture, Tokyo Institute of Technology, 2-12-1 Ōokayama, Meguro-ku, Tokyo 152-8550, Japan. Email: takeuchi.t.ab@m.titech.ac.jp

[3]Assistant Professor, Dept. of Architecture, Tokyo Institute of Technology, 2-12-1 Ōokayama, Meguro-ku, Tokyo 152-8550, Japan. Email: terazawa.y.aa@m.titech.ac.jp

[4]Manager, Nippon Steel Engineering, Osaki Center Build., 1-5-1 Osaki, Shinagawa-ku, Tokyo 141-8604, Japan. Email: terashima.masao.mx4@eng.nipponsteel.com

Note. This manuscript was submitted on August 31, 2020; approved on July 20, 2021; published online on November 16, 2021. Discussion period open until April 16, 2022; separate discussions must be submitted for individual papers. This paper is part of the ***Journal of Structural Engineering***, © ASCE, ISSN 0733-9445.

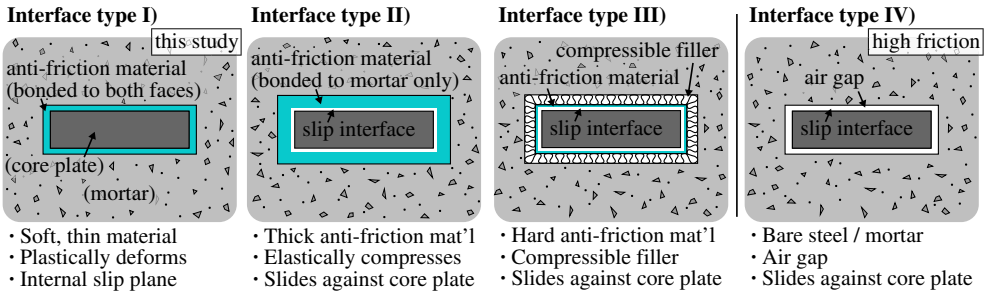

Fig. 1. Types of BRB debonding interfaces.

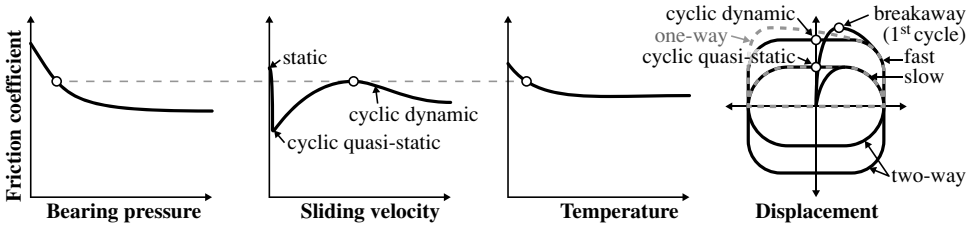

Fig. 2. Schematic of friction coefficient dependencies in polymers.

the countersurface (Stachowiak and Batchelor 2014), while viscoelasticity may result in a greater response when loaded from an at-rest state (Kasai and Nishizawa 2010; Kumar et al. 2015). Dynamic breakaway effects are uniquely important for BRBs because the core straightens and contracts during tension half-cycles, causing contact to recur each compression half-cycle (one-way sliding), which differs from conventional reciprocating motion with continuous contact (two-way sliding). These dependencies are depicted schematically in Fig. 2.

The objective of this study is to experimentally quantify the friction coefficient of a soft, thin polymer of Interface type I (Fig. 1), at full scale and with realistic sliding conditions. First, the plausible range of bearing pressures, slip velocities, and slip displacements are developed from a preliminary parametric numerical study. Next, the test rig is introduced, and results are presented from a comprehensive program of one-way and two-way sliding tests. These data are used to develop a nonlinear pressure–velocity–displacement–dependent friction model. Finally, implications for modeling higher-mode buckling and friction, qualification, and testing of BRBs are discussed.

Pressure, Velocity, and Distance Characterization

No codified test protocol currently exists to systematically obtain the friction coefficient for BRB debonding interfaces, and the contact and slip demands that may plausibly be encountered in practice are not well understood. Therefore, a parametric study (Sitler and Takeuchi 2021) of 576 Abaqus/Explicit 2017 models (Smith 2017) was postprocessed to characterize the maximum and minimum bearing pressures, slip velocities, and slip distances and narrow the test specification.

Two simplifications were adopted. First, because the proposed nonlinear friction model was not known a priori, constant-friction Coulomb models were adopted, following current practice. Additional validation models were later analyzed using the proposed nonlinear friction model, but they produced only minor changes. This confirmed that while many BRB response parameters and failure modes may be sensitive to friction, the contact and slip demands are not. Secondly, half-length two-dimensional (2D) models were adopted to improve runtime. These conservatively capture the demands at the plate edges, as three-dimensional (3D) anticlastic plate deformation reduces contact over the middle of the rectangular core plates (Sitler and Takeuchi 2021). BRB failure modes, such as global buckling and bulging, were not modeled to avoid arbitrarily limiting the analysis by a design-specific capacity.

A wide range of core properties were investigated in the preliminary numerical study, including different core steel grades (LY100, LY225, SN400B, SN490B, SA440B, SA700), yield lengths (L_p = 2, 6, 10, 14 m), thicknesses (t_c = 16, 25, 40 mm), debonding gaps ratios (s_w/t_c = 0.01, 0.03, 0.05, 0.1) and friction coefficients (μ = 0.1, 0.3). The subsequent validation study reanalyzed the SN400B, L_p = 2, 6 or 10 m and t_c =16, 25 or 40 mm models using the nonlinear friction model with s_w = 0.5, 1.0 or 2.0 mm. Each model consisted of a fine mesh ($t_c/5 \times t_c/5$) of reduced integration shell elements (CPS4R) over a depth t_c and length $L_p/2$. The mesh was offset by debonding gaps (s_w, per face) to upper and lower analytical rigid surfaces representing a stiff, elastic restrainer. Hard friction contact was assigned but validated against a tabular hardening contact, which was also used for the nonlinear friction models. Half the BRB axial displacement ($\delta/2$) was applied at the free end, while the opposite end was restrained to represent a midspan shear key. The protocol consisted of two cycles each at an average axial strain of $\bar{\varepsilon} = \delta/L_p$ = 0.5%, 1.0%, 1.5%, 2.0%, 2.5%, and 3.0%, which was applied sinusoidally at a 2 s period for the velocity-dependent models. The constitutive material models and further details are provided in Sitler and Takeuchi (2021).

Bearing Pressure

The bearing pressure (σ_N) was calculated by averaging the Abaqus field output CPRESS for the nodes in contact at each wavecrest, and the mean is shown in Fig. 3 at three strain levels. The bearing pressure was primarily determined by the debonding gap ratio (s_w/t_c) and was not meaningfully correlated with the other dimensions, location along the yield length, nor friction model. The low yield point (LY100, LY225) and mild steels (SN400B, SN490B)

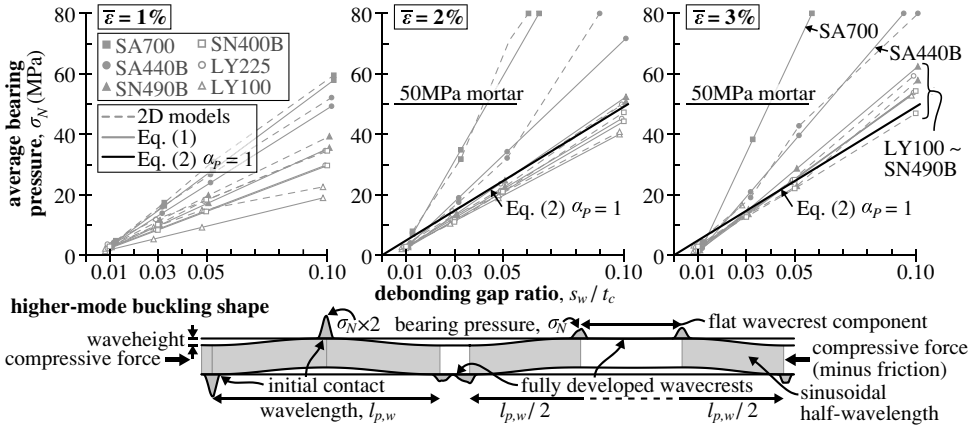

Fig. 3. Average bearing pressure at higher-mode buckling wavecrests.

stabilized to similar bearing pressures at large strains ($\bar{\varepsilon}$>2%), while the high-strength steels (SA440B, SA700) with yield strengths exceeding $f_y > 400$ MPa produced higher bearing pressures. This was due to the mechanics of higher-mode buckling and material properties, which are explained as follows.

Normal force is generated at the higher-mode buckling wavecrests during compression half-cycles due to the core axial force acting at an incline determined by the sinusoidal wavelength and wave height (Fig. 3). Both are smallest at the core ends and gradually increase along the yield length as friction sheds force from core to the restrainer, which reduces the compressive stress (σ_c) and strain (ε_c). The wave height equals the total as-built debonding gap ($2s_w$) less Poisson expansion of the core ($-\nu_p|\varepsilon_c|t_c$, where $\nu_p = 0.5$ is the plastic Poisson ratio), while the sinusoidal wavelength ($l_{p,w}$) is a function of the material-specific axial stress (σ_c) and tangent stiffness (E_t) and may be estimated as $l_{p,w}/t_c \approx 2\pi\sqrt{(E_t/3\sigma_c)}$ (Sitler and Takeuchi 2021). The lower tangent stiffnesses of the high-strength (SA440B, SA700) and low-yield-point (LY100, LY225) steels result in shorter wavelengths than SN400B and SN490B, while the axial stress increases with the steel grade. This suggests that the bearing pressure will be substantially higher for SA400B and SA700, but almost identical for LY100, LY225, SN400B, and SN490B, which is consistent with the numerical results.

Based on this understanding, an analytical estimate of the wavecrest bearing pressure (σ_N) is given by Eq. (1), where the compressive stresses (σ_c), wave heights ($2s_w - \nu_p|\varepsilon_c|t_c$), and sinusoidal wavelengths ($l_{p,w}$) may be obtained by cycling the engineering stress-strain curve to $\varepsilon_c = -\bar{\varepsilon}$. The contact length ($l_c$) was complex because highly concentrated initial contact tended to be alleviated as the wavecrests flattened, until new waves eventually formed via snap-through buckling. Nevertheless, the total contact length was about $l_c \approx 0.9t_c$ for fully developed wavecrests, but about half this length at initial contact (Fig. 3). Both the average and peak bearing pressure may be obtained as

$$\sigma_N \approx 2\sigma_c \cdot \frac{t_c}{0.5l_{p,w}} \cdot \left(\frac{2s_w}{t_c} - \nu_p|\varepsilon_c|\right) \cdot \frac{t_c}{l_c} \tag{1}$$

Given that the debonding gap ratio (s_w/t_c) was the dominant parameter at large strains for most steel grades, Eq. (1) may be further simplified to Eq. (2), where the pressure concentration factor (α_P) may be taken as $\alpha_P = 1$ for fully developed wavecrests with $l_c = 0.9t_c$ and $\alpha_P = 2$ at initial contact. Eq. (2) may be used by engineers to estimate the wavecrest bearing pressure

$$\sigma_N \approx \alpha_P \cdot 50 \text{ MPa} \cdot 10\frac{s_w}{t_c} \quad (\text{for } f_y < 400 \text{ MPa}, \bar{\varepsilon} > 2\%) \tag{2}$$

As the most common debonding gap ratios ($0.01 < s_w/t_c < 0.05$) produced bearing pressures anywhere from $\sigma_N = 5$–50 MPa (with $\alpha_P = 1$–2), values up to the mortar's compressive strength were considered for the friction test. Note that the bearing pressure is not a function of friction.

Slip Velocity

Next, the slip velocity was calculated from the slip rate (FSLIPR), but was nearly equal to the instantaneous rate of relative axial deformation between the core and restrainer at the contact node in question. The relative motion is directly determined by the externally applied stroke displacement (δ_{stroke}) at the core ends and gradually decreases to zero at the fixity point, which is typically a midspan shear key. Assuming that the axial restrainer and connection deformations are negligible and structural drift is predominately shear, δ_{stroke} is given by Eq. (3), where Δ is the interstory drift angle, H_{wp} the workpoint height, and θ_{BRB} the horizontal inclined angle (Fig. 4). With a competent shear key dividing the axial displacement evenly between each end and $\theta_{\text{BRB}} = 30°$–50°, the displacement stroke at each end is just 30% to 45% of the horizontal story displacement:

$$\delta_{\text{stroke}} = 0.5 \cdot \Delta \cdot H_{wp} \cdot \cos\theta_{\text{BRB}} \tag{3}$$

The maximum slip velocity (V_{slip}) at the core ends is then equal to the stroke velocity (V_{stroke}), which is given as follows by Eq. (4) for a structure vibrating in a sinusoidal motion with period T:

$$V_{\text{slip}} = V_{\text{stroke}} = \frac{\pi}{2} \cdot \frac{4\delta_{\text{stroke}}}{T} = \pi\frac{\Delta \cdot H_{wp} \cdot \cos\theta_{\text{BRB}}}{T} \tag{4}$$

The slip velocity distribution along the core is depicted in Fig. 4 for the final cycle of an example model with SN400B, $t_c = 25$ mm, $L_p = 2$ m, $s_w/t_c = 0.05$, and $\mu = 0.3$. The longitudinal distribution was sublinear because the axial deformation rate decreased along the core as friction shed force to the restrainer. Thus, most wavecrests experience much lower slip velocities, even during dynamic earthquake events (Fig. 4). Because wavecrests along the entire core contribute to the cumulative friction force, the test considered quasi-static to peak stroke velocities, which are independent of friction.

Single-Cycle Slip Distance

Unlike the slip velocity, the slip distances included an essentially random component and so must be assessed probabilistically.

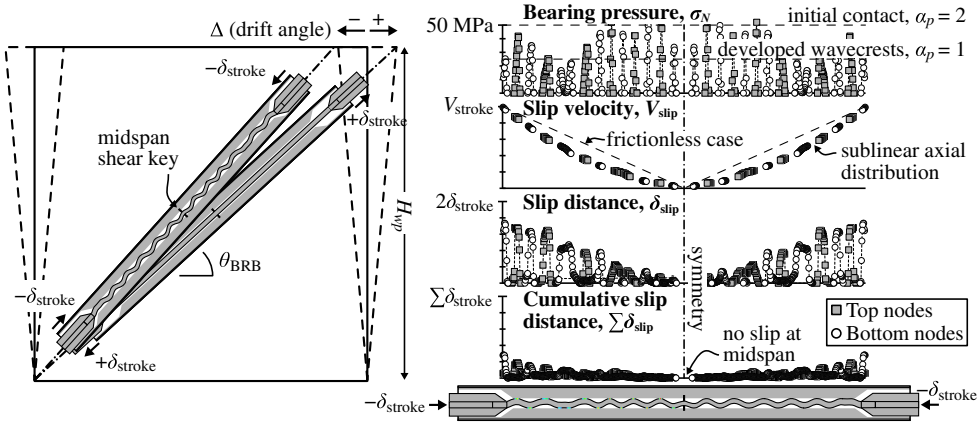

Fig. 4. BRB frame and core kinematics.

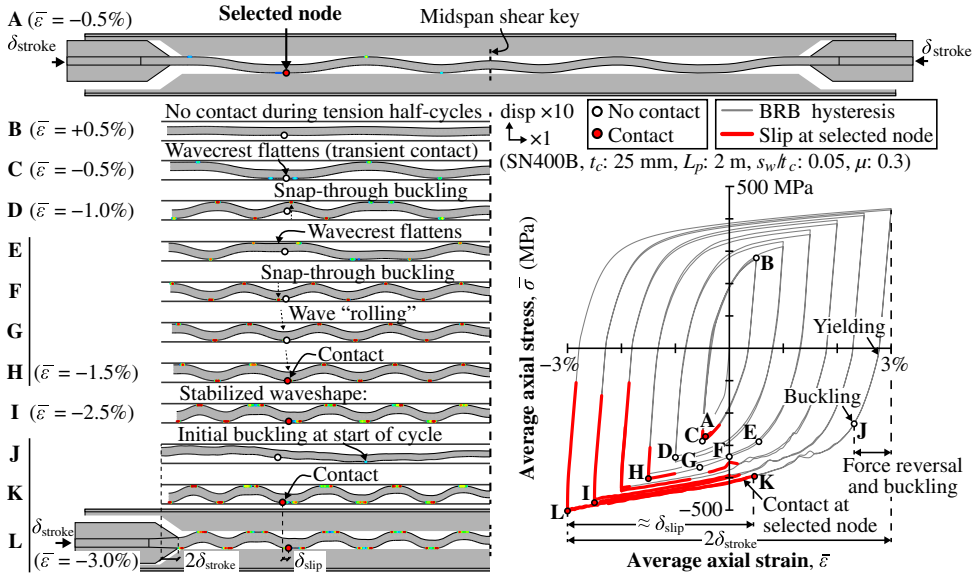

Fig. 5. Higher-mode buckling progression.

Specifically, the maximum slip distance (δ_{slip}) over a compressive half-cycle from $+\delta_{stroke}$ to $-\delta_{stroke}$ was always less than the relative displacement between the core and restrainer ($2\delta_{stroke}$) since points were ever only occasionally in contact. This was due to the small deformation required for force reversal and initiation of buckling, and to the constant change in the higher-mode buckling shape. Following the arbitrarily selected point in Fig. 5, the higher-mode buckling waves occasionally *rolled* along the core toward midspan (G and H), while the wavecrest flattening alleviated contact at the center of each wavecrest and eventually permitted new waves to form via snap-through buckling (D and F). Therefore, no point was ever in contact for a full cycle, and the points in contact constantly changed from cycle to cycle. Nevertheless, the critical point experiencing the maximum slip was usually, but not always, located at the endmost wavecrest.

Cumulative Slip Distance

The maximum single-cycle (δ_{slip}) and cumulative ($\sum\delta_{slip}$) slip displacements were obtained from FSLIPEQ and are depicted in Fig. 6, normalized by $2\delta_{stroke}$ or $\sum\delta_{stroke}$. These were always significantly less than the applied stroke but increased as the higher-mode buckling shape stabilized during the large-amplitude cycles later in the loading protocol. Furthermore, no correlation was observed with the steel grade or core dimensions. The variation across all models followed a normal distribution, and the final-cycle mean slip ratios and COVs for the preliminary 576 models are given by Eqs. (5) and (6)

$$\delta_{slip} = 0.57 \cdot 2\delta_{stroke} \quad (COV = 0.12) \tag{5}$$

$$\sum\delta_{slip} = 0.19 \cdot \sum\delta_{stroke} \quad (COV = 0.22) \tag{6}$$

The nonlinear friction model slightly increased the duration of contact at some points and resulted in slip ratios of $\delta_{slip} = 0.62{\cdot}2\delta_{stroke}$ (COV = 0.09) and $\sum\delta_{slip} = 0.22\sum\delta_{stroke}$ (COV = 0.14), or one standard deviation above the original results. This information was not available a priori but is offset by conservatism in the original results (i.e., 5%–20% of FSLIPEQ occurs at negligible bearing pressures, and the original test specification rounded up the target displacements), and so is not considered further. Nevertheless, future studies may consider these higher slip ratios.

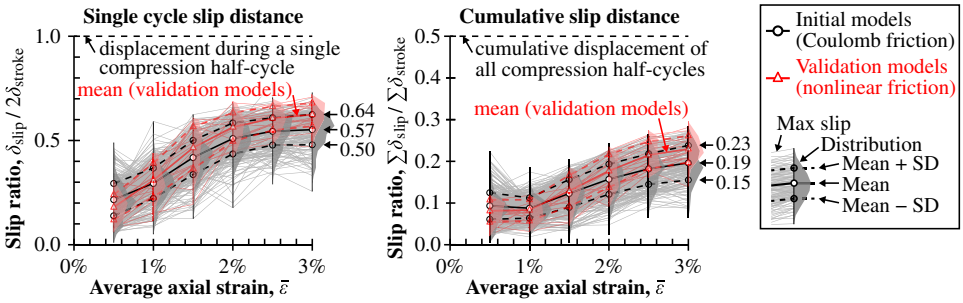

Fig. 6. Normalized single-cycle and cumulative slip distances.

A probabilistic estimate of the maximum slip displacement at the core ends may then be estimated from the stroke displacement imposed by a BRB qualification protocol. AISC 341-16 prescribes a BRB qualification protocol of $2 \times 0.5\Delta_{bm}$, $2 \times 1.0\Delta_{bm}$, $2 \times 1.5\Delta_{bm}$, $2 \times 2.0\Delta_{bm}$, $2 \times 1.5\Delta_{bm}$, where Δ_{bm} is the design drift, which is permitted to vary from 1% to 2.5% for normal buildings (AISC 2016). Nevertheless, well-designed BRBs exhibit sufficient fatigue capacity to withstand multiple design-level events and so even larger cumulative slip displacements are of interest.

The cumulative slip displacement at fracture may be obtained from the empirical low cycle fatigue (LCF) curves developed for BRBs, which are reduced from the uniaxial base material capacities due to higher-mode buckling, friction-induced strain ratcheting, triaxiality and strain concentration. In the plastic regime, the number of cycles to fracture (N_f) is given by Eq. (7) as a function of the Coffin-Manson exponent (m) and index strain range ($\Delta\varepsilon_0$). This study adopted $m = 0.49$ and $\Delta\varepsilon_0 = 0.2048$ (Yoshikawa et al. 2010), while the average axial strain range of $2\bar{\varepsilon} = 2\delta_{stroke}/L_p$ was computed at the design drift ($\Delta = \Delta_{bm}$) using Eq. (3), assuming that $L_p < 0.8L_{wp}$ and $L_{wp} = H_{wp}/\sin\theta_{BRB}$. The cumulative slip displacement at fracture was then obtained from Eq. (6), but with the cumulative stroke displacement [Eq. (8)] estimated by cycling to fracture at the average axial design strain

$$N_f = \left(\frac{2\bar{\varepsilon}}{\Delta\varepsilon_0}\right)^{-1/m} \tag{7}$$

$$\sum \delta_{stroke} = 4\delta_{stroke}N_f \tag{8}$$

Characteristic Slip Velocity and Distances

The maximum slip velocities and slip displacements at the core end were calculated from Eqs. (3)–(8) for several archetype structures in Table 1. The maximum slip velocity was typically on the order of $V_{slip} = 50$–200 mm/s but increased up to 500 mm/s for short period structures with long BRBs (e.g., warehouses). Similarly, the maximum slip distance varied from $\delta_{slip} = 30$–80 mm, while the cumulative slip during the compression half-cycles was less than $\sum\delta_{slip,AISC} < 0.5$ m for the AISC 341-16 protocol. The cumulative slip at fracture increased to $\sum\delta_{slip,LCF} < 1$–$2$ m for most archetypes but was sensitive to the yield length and may exceed 4 m for long BRBs subjected to dozens or hundreds of small-amplitude low cycle fatigue cycles.

Considering that the friction force accumulates from all wave-crests along the entire yield length, slip values from zero up to the calculated maximums are of interest, while bearing pressures were previously shown to vary from $\sigma_N = 3$–50 MPa, depending on the debonding gap ratio. Therefore, the characteristic demands for low- and midrise structures include slip velocities from $V_{max} = 0$–200 mm/s, single-cycle slip distances from $\delta_{slip} = 0$–80 mm and one-way cumulative slip distances from $\sum\delta_{slip} = 0$–2.0 m. Note that the velocities applied in the experiment were slightly lower, but the friction velocity-dependency saturated well below 200 mm/s. Additionally, although cyclic heating has a small beneficial effect on the friction coefficient (Kumar et al. 2015), it is difficult to monitor the debonding material temperature and the sides were left open to permit visual monitoring, limiting the potential temperature gain. Consequently, temperature dependency was outside the scope of this study, other than to report the friction coefficient at the third cycle.

Experimental Setup

Test Rig

A unique test rig (Fig. 7) was designed to accommodate dynamic horizontal reciprocating motion while applying a static, load-controlled vertical force (i.e., compression half-cycles) or displacement-controlled lifted position for the return motion (i.e., tension half-cycles). This was achieved using a lower horizontal actuator that drove the slide table, and an upper vertical actuator and jointed horizontal load cell stabilized by removable ball bearings and cylindrical guide plates. This test setup was capable of ±150 mm/s, ±300 mm, and ±500 kN in the horizontal direction, and +25 mm/ − 5 mm and +500 kN in the vertical

Table 1. Typical slip velocities and slip distances

Archetype structure	H_{wp} (m)	θ_{BRB} (degrees)	T (s)	Δ_{bm} (rad) (%)	δ_{stroke} (mm)	V_{slip} (mm/s)	δ_{slip} (mm)	$\sum\delta_{slip,AISC}$ (m)	$\sum\delta_{slip,LCF}$ (m)
Warehouse	8.0	45	1.0	2.5	71	444	81	0.5	2.5
Low-rise	3.5	45	1.0	2.5	31	194	35	0.2	1.1
Midrise A	3.5	45	2.0	2.5	31	97	35	0.2	1.1
Midrise B	3.5	30	2.0	2.5	38	119	43	0.3	1.8
Midrise C	3.5	45	2.0	2.0	25	78	28	0.2	1.4
Tall building	10.0	45	4.0	2.0	71	111	81	0.5	3.9

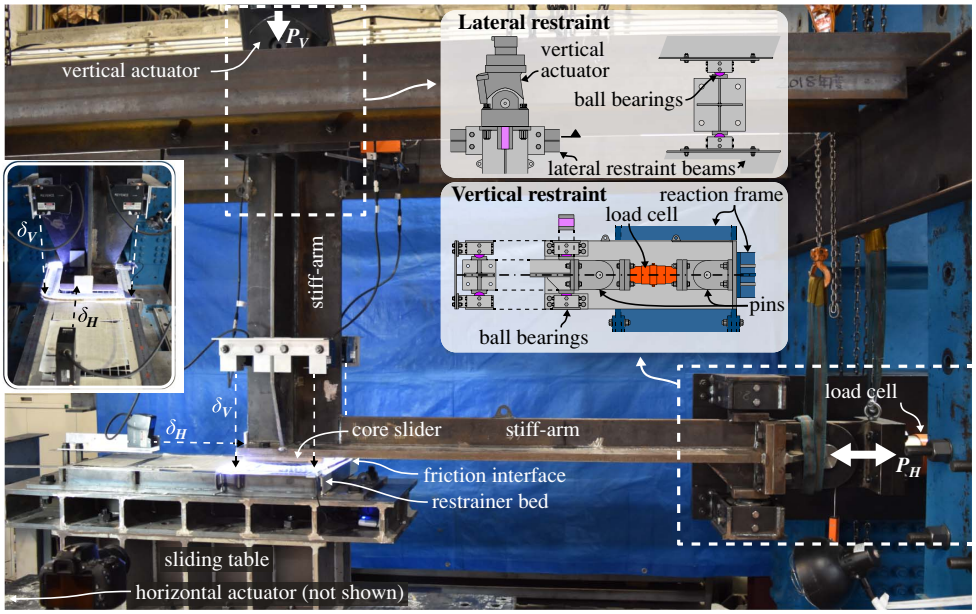

Fig. 7. Test setup.

direction, with positive values referring to compressive bearing pressures, and down/rightwards movement of the upper surface. Testing was conducted by the authors from October 2019 to January 2020 at the Tokyo Institute of Technology.

Test Specimens

Eight specimens were prepared, each consisting of a curved core slider bolted to the upper stiff-arm assembly and a mortar-filled restrainer bed bolted to the lower sliding table (Fig. 8). The debonding materials were applied after curing and leveling the mortar to a ±1 mm finish, or after curing the mortar for 6 h, leveling and rewetting to form a bond with the textile, where applicable. Stiffened cover plates were fixed with 8 × M6 Grade 4.6 bolts to introduce a 0.5 MPa hold-down pressure representing the hydrostatic pressure imposed by wet mortar, but they were removed the morning of the test to mark out a white 20 × 20 mm grid.

The core slider geometry was designed to capture friction scale effects and may reasonably represent any wavecrest of a rectilinear core plate. Each core slider featured a 50 × 100 mm apparent contact area surrounded by surfaces inclined at 1:5 and finished to a 100 mm radius in the direction of sliding, and 1:4 inclined surfaces finished to a 25 mm radius on the other two sides. The 50 mm contact length helped to promote uniform bearing pressures in the presence of the test rig eccentricities. To ensure a consistent finish, only four core sliders were fabricated, and each was cleaned with oil and sanded using a coarse 120-grit sandpaper prior to each test to replicate an unpainted core plate with mill scale removed. Nevertheless, plowing wear dominated, minimizing the influence of corrosive wear if oxides were present (Stachowiak and Batchelor 2014).

Two types of restrainer beds were employed with a 736 or 838 mm long mortar surface, which permitted multiple test positions per specimen. The restrainer beds of three specimens (N-1, A1-1, and A1-2 in Table 2) were elevated on steel angles, cast with 25 MPa concrete (A1-1 and A1-2) or 50 MPa mortar (N-1), and later reused for bulging tests, which are not reported in this paper. The remaining five specimens employed nonelevated restrainer

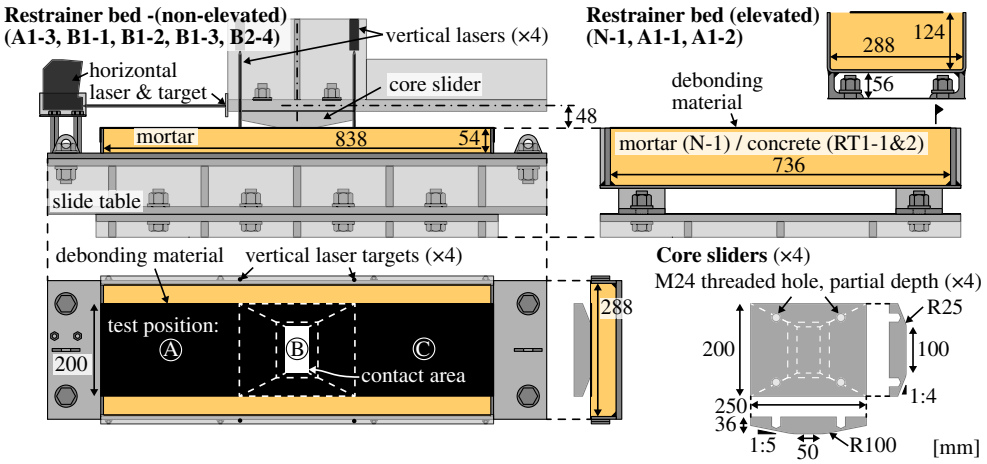

Fig. 8. Test specimens.

Table 2. Test specimen summary

	Debonding material		Test conditions		Test position A		Test position B		Test position C	
			Date	TA	σ_N	$\pm\delta_H$	σ_N	$\pm\delta_H$	σ_N	$\pm\delta_H$
ID		mm		°C	MPa	mm	MPa	mm	MPa	mm
N-1	—[a]	—	November 6, 7	19–22	10, 20	TW 20	10	OW 20	30	TW 20
A1-1	Textile/polymer[b,c]	1	November 1	21–25	10	TW 20	20	TW 20	(Practice run)	
A1-2	Textile/polymer[c,d]	1	November 13, 15	15–18	10	OW 20	10	OW 40	30	OW 20
A1-3	Polymer/textile[a,e]	1	October 28, 29	15–22	10–45	TW 20	10	TW 20[f]	(Practice run)	
B1-1	Polymer[a]	1	November 16, 20	13–20	10	TW 20	20	TW 20	30	TW 20
B1-2	Polymer[a]	1	December 17, 18	8–17	10	TW 20	25	TW 20	30	OW 20
B1-3	Polymer[a]	1	January 22, 23	5–8	3, 5, 40	TW 20	10–40	OW 20	20	OW 40
B2-4	Polymer[a]	2	January 23, 27	6–7	3, 5, 40	TW 20	10	TW 20	30	TW 20

Note: TA = ambient temperature; TW = two-way sliding; and OW = one-way sliding.
[a]49.5 MPa (28-day) mortar.
[b]21.5 MPa (9-day) concrete.
[c]A1-1&2: polymer with textile facing mortar.
[d]25.5 MPa (13-day) concrete.
[e]A1-3: polymer with textile facing core slider.
[f]A1-3: 10 calibration sets, followed by 6×5, 13×10, and 10×50 cycles at $V_{max} = 80$ mm/s.

beds with 50 MPa mortar (54% water/cement, 5 mm crushed sand). The mortar was cast on September 13, 2019, and the concrete on October 23, producing the cylinder strengths reported in Table 2.

The debonding interfaces are denoted in Table 2 by the material (N, A, or B), nominal thickness (1 or 2 mm), specimen number (1–4) and position (A–C). As a control, one specimen (N-1) was tested with no debonding material (Interface type IV), while the debonded specimens were of Interface type I. Three of these featured a soft polymer with textile backing facing the mortar (A1-1, A1-2) or core slider (A1-3) and a combined 1 mm thickness, while another four employed 1 mm (B1-1, B1-2, B1-3) or 2 mm (B2-4) of a soft polymer. These were selected to be representative of the unique debonding materials used in a variety of BRBs from international practice and academia, and were provided by a major BRB supplier.

Loading Protocol

A standard protocol was developed consisting of 15 sets of 4 cycles (Table 3), with a minimum 5 min rest period between each set. Each test position targeted a fixed bearing pressure ($\sigma_N = 3$, 5, 10, 20, 25, 30, 40, or 45 MPa) and horizontal displacement amplitude ($\delta_H = \pm 20$ or ± 40 mm), although smaller amplitudes ($\delta_H/10$, $\delta_H/4$ and $\delta_H/2$) were applied in the first three breaks in sets. The target velocity was varied in subsequent sets ($V_{max} =$ 0.8–125 mm/s), but a reference velocity of $V_{max,0} = 30$ mm/s was applied every third set to track the effect of the cumulative slip distance. Additional sets were applied at $V_{max,0}$ with lower bearing pressures for B1-3A, B1-3B, and B2-4A, while A1-3B was subjected to an extended protocol of over 650 cycles at $V_{max} =$ 80 mm/s, and the earlier (N, A1) specimens omitted the low-velocity sets below 10 mm/s.

Two different sliding procedures were used, denoted as *two-way sliding* and *one-way sliding*. For two-way sliding, the vertical load was slowly applied once and then held constant throughout the entire test. Sequential sets of reciprocating sinusoidal motion were applied, with the first half-cycles also applied sinusoidally to avoid an impulse. One-way sliding also imposed dynamic horizontal reciprocating motion, but the vertical force was reapplied at the start of each cycle and only imposed during the motion in one direction. This represents the fact that BRB higher-mode buckling wavecrests only form during compression half-cycles, and contact at the wavecrests is removed as the core straightens and contracts during the tension half-cycles. Each one-way cycle started at $-\delta_H$; contact was initiated using displacement control and the full vertical force applied using load control. The core slider was then displaced horizontally in a sinusoidal motion from $-\delta_H$ to $+\delta_H$ over a duration $T/2$, lifted and returned from $+\delta_H$ to $-\delta_H$ before immediately starting the next cycle. The distance lifted for the return motion was to the point of zero load (i.e., as-built condition), plus an additional

Table 3. Example standard loading protocol (B1-2C: $\sigma_N = 30$ MPa, $\delta_H = \pm 20$ mm)

Set	Cycles (total)	P_V kN	σ_N MPa	δ_H mm	$\sum \delta_H$[a] m	T s	V_{max}[b] mm/s	Set	Cycles (total)	P_V kN	σ_N MPa	δ_H mm	$\sum \delta_H$[a] m	T s	V_{max}[b] mm/s
1[c]	4 (4)	150	30	±2	—	0.4	30	9	4 (36)	150	30	±20	0.96	1.0	125
2[c]	4 (8)	150	30	±5	—	1.0	30	10	4 (40)	150	30	±20	1.12	4.0	30
3[c]	4 (12)	150	30	±10	—	2.0	30	11	4 (44)	150	30	±20	1.28	160	0.8
4	4 (16)	150	30	±20	0.16	4.0	30	12	4 (48)	150	30	±20	1.44	8.0	15
5	4 (20)	150	30	±20	0.32	80	1.5	13	4 (52)	150	30	±20	1.60	4.0	30
6	4 (24)	150	30	±20	0.47	2.0	60	14	4 (56)	150	30	±20	1.76	40	3.0
7	4 (28)	150	30	±20	0.64	4.0	30	15	4 (60)	150	30	±20	1.92	4.0	30
8	4 (32)	150	30	±20	0.80	16	7.5	—	—	—	—	—	—	—	—

Note: σ_N and δ_H changed at each test position. Duration ≈ 3 h 40 min, including rest periods.
[a]Cumulative slip displacement in positive direction only, excluding break in sets.
[b]Target slip velocity, $V_{max} \approx \pi/2 \times 4\delta_H/T$.
[c]Break in sets.

+0.5 mm to represent tensile Poisson contraction of the core. While only one-way sliding occurs in real BRBs, two-way sliding retains substantial parallels given the similar horizontal motion and so was used to establish most of the friction coefficient dependencies. Two-way sliding was also used for validation purposes and corresponds to the stabilized dynamic friction coefficients commonly cited in the literature.

Instrumentation

The vertical (i.e., normal) (P_V) and horizontal (i.e., shear) (P_H) forces were measured using load cells in the stationary upper test rig to exclude the test rig friction. No postprocessing was required for the normal force, while a 25 Hz lowpass filter was applied to the shear force data. The horizontal pins had a total slack of 1.5 mm, which introduced small impact forces at each load reversal, but these accounted for less than 20% of the amplification in the first cycle and rapidly decayed. Unless stated otherwise, the friction coefficient ($\mu = P_H/P_V$) is always reported at the zero-displacement intercept (i.e., peak velocity) of the third cycle, with the positive and negative intercepts averaged for the two-way sliding tests. The average bearing pressure (σ_N) was taken as P_V divided by the apparent contact area (50 × 100 mm), although in-plane rotational slack of the stiff-arm assembly and wear resulted in a slightly uneven contact surface. Finally, the relative vertical (δ_V) and horizontal (δ_H) displacements at the sliding interface were directly measured using lasers (one horizontal and four vertical), and the maximum slip velocity ($V_{\max}$) confirmed from the slip displacement rate obtained using a fifth-order Savitzky-Golay polynomial with a $T/8$ window.

Experimental Results

Bare Steel-Mortar Test Results

A bare steel-mortar specimen (N-1) of Interface type IV was tested as a control. This specimen exhibited a constant friction coefficient of $\mu \approx 0.75$ at zero displacement in all cycles, but neither pressure nor velocity dependency (Fig. 9). The friction hysteresis was rectangular during the first few sets, which is characteristic of Coulomb friction. However, the abraded surface began to spall during the 6th set (22nd cycle), even with a bearing pressure of just $\sigma_N = 20$ MPa (i.e., 40% of the mortar compressive strength). The spalled mortar grains were then plowed into a slope, inclining the tangent plane and increasing the shear force, which is visible as small bumps in Fig. 9.

Spalling increased the vertical displacement by about 0.5 mm per four cycles, which would significantly increase the higher-mode buckling amplitude. Although stress concentrations may have occurred at the leading edges, none of the corresponding debonded specimens crushed at these low pressures, nor did any spall even at much higher pressures. It is more likely that damage accumulated from the large longitudinal shear stresses in the unreinforced mortar because the large, spalled flakes were inconsistent with a crushing failure. Regardless of the specific cause, the high friction coefficient and spalling are significant performance limitations because they increase the compressive overstrength force and risk of restrainer bulging, and so an antifriction debonding material (Interface types I, II, and III) is strongly recommended for mortar-filled steel tube BRBs.

Two-Way Sliding Test Results

The friction coefficients achieved for the debonded Interface type I specimens are shown in Fig. 10 for a range of bearing pressures, slip velocities and cumulative slip distances. Although only a subset of the B1 (1 mm polymer) specimen data is shown, the A1 (1 mm polymer with textile) and B2 (2 mm polymer) specimens exhibited similar performance. Comprehensive third-cycle friction coefficients are illustrated later in Fig. 15 and complete results in Sitler (2021). The friction coefficient increased at low bearing pressures, doubled from $\sigma_N = 20$ to 3 MPa, and then slightly decreased at higher pressures. Friction coefficients were recorded between $\mu = 0.03$ and 0.05 during quasi-static loading ($V_{\max} < 1.5$ mm/s), increased to $\mu = 0.06$–0.10 at $V_{\max,0} = 30$ mm/s, and then slightly decreased at higher velocities with high bearing pressures, likely due to increased cyclic heating. Furthermore, the friction coefficient was significantly amplified during the first cycle of the high-velocity tests, but there was negligible amplification at the first cycle of the quasi-static tests. This is discussed further in the context of the one-way sliding results.

An extended dynamic protocol was applied to the A1-3B specimen with 5, 10, and 50 cycle sets at $V_{\max} = 80$ mm/s to saturate the potential cyclic heating and give an indication of the temperature dependency. Extrapolating to exclude the first-cycle dynamic amplification, the friction coefficient experienced an average 30% reduction from the 1st to 10th cycles, but half of this total reduction occurred in the first 3 cycles and there was negligible change after the 10th cycle. Also, the debonding material formed a hard, crystalline residue by the end of the test and may have melted.

Two-Way Sliding Test Results: Wear Effect

A unique wear effect was observed due to the mortar countersurface, which is weaker than the steel countersurfaces more commonly used in antifriction applications. As depicted in Fig. 11, the transfer material fully coated both countersurfaces and exhibited significant plowing wear. This was accompanied by an increased friction coefficient (Fig. 10), which was tracked at the

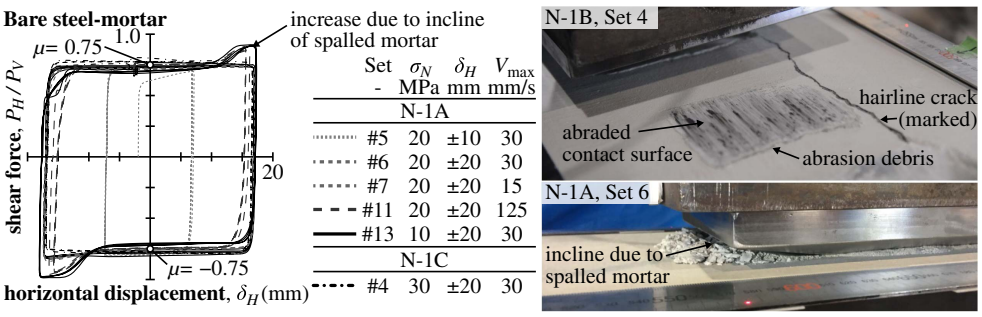

Fig. 9. Friction hysteresis, bare steel–mortar.

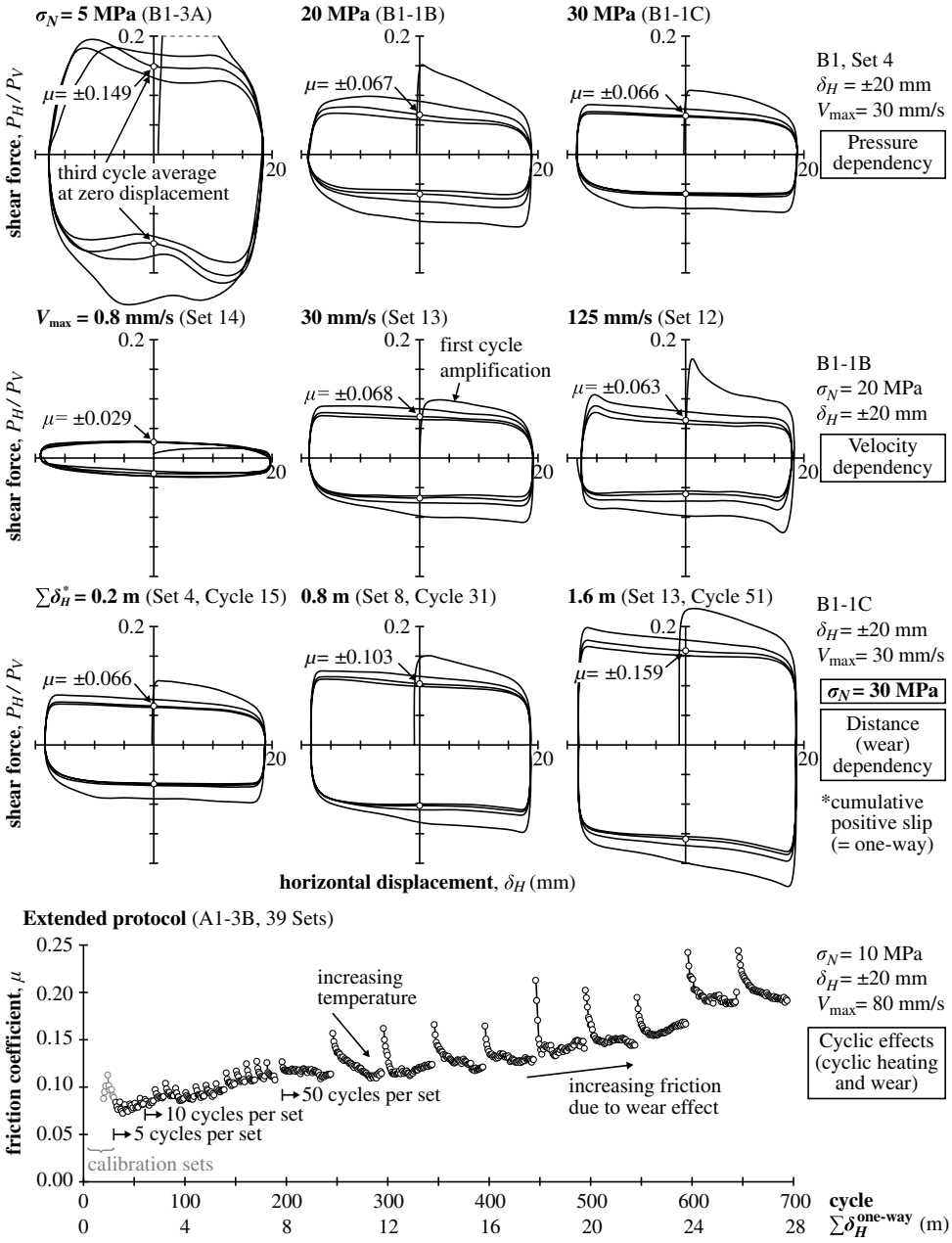

Fig. 10. Friction hysteresis, two-way sliding.

reference velocity $V_{\max,0}$ every third set and increased linearly with cumulative slip distance, higher bearing pressure, and thinner debonding material. Although wear does not usually immediately increase the friction coefficient, this appeared to be a system effect, as small patches of exposed mortar were observed during the visual inspections. The bare steel and mortar exhibited a constant friction coefficient of $\mu = 0.75$, and so these patches increased the smeared friction coefficient. However, the previously displaced debonding material eventually resurfaced the exposed mortar, creating a self-healing effect that limited the increase to a *wear coefficient* of $\mu_W < 0.15$.

This upper bound wear coefficient was also tested in Specimen A1-3B by applying an extended protocol with over 28 m of positive sliding, which is about 10 times the expected cumulative slip distance at fracture for a high-performance BRB and so would never be experienced in practice. Nevertheless, while the friction coefficient continued to gradually increase set to set, the wear contribution always remained below $\mu_W < 0.15$ and the total friction coefficient below $\mu < 0.25$, which is one third of the friction coefficient of the bare steel-mortar control specimen. High bearing pressures ($\sigma_N = 45$ MPa) applied to the A1-3A specimen caused localized crushing. The dislodged, interspersed mortar grains temporarily increased the friction coefficient by 0.15 to $\mu = 0.22$, but this subsequently recovered, suggesting that the $\mu_W < 0.15$ limit also applies to crushed mortar.

The wear effect was also influenced by the debonding material composition and thickness. Specifically, mortar patches were exposed earlier for thinner polymers, which had less transfer material available to resurface the exposed mortar patches. This may be observed by comparing the otherwise identical 1 mm (B1-3A) and 2 mm (B2-4A) specimens in Fig. 12. These exhibited identical pressure and velocity dependencies, but the friction coefficient

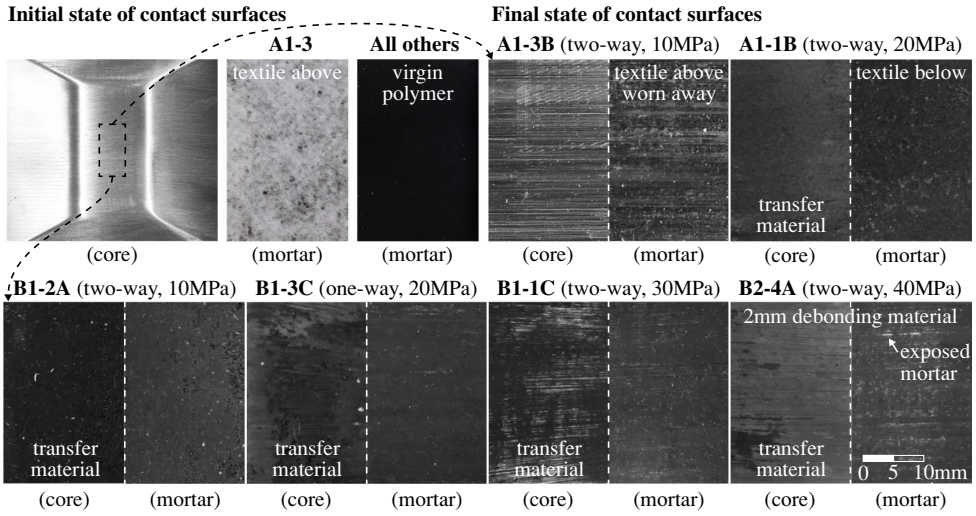

Fig. 11. Final state of contact slip surfaces.

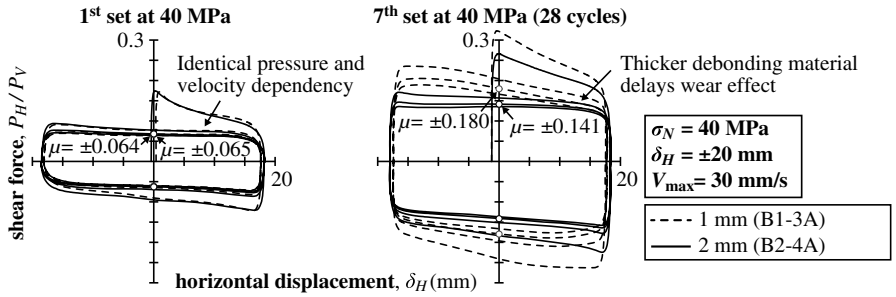

Fig. 12. Friction hysteresis, thick debonding material.

increased 50% faster for the thinner B1-3A specimen. The bearing pressure at which wear began to increase the friction coefficient was a function of thickness, while the rate of increase was directly proportional to how much the applied pressure exceeded this *wear-initiating bearing pressure*.

Conversely, the textile backing of the A1-1 and A1-2 specimens tore just outside the contact area. While this did not affect the friction coefficient in this test, the large, exposed patches may significantly degrade the performance should the core slide over this area. Conversely, the A1-3 specimen had the textile backing placed upside down facing the core slider. The textile tore near the center and was subsequently ejected from the contact area, causing a spike in the friction coefficient for several cycles (Fig. 10), until the transfer material on the mortar countersurface was able to resurface the exposed patch. Therefore, the effect of textile backing is neutral at best and potentially detrimental, as a large area of high-friction bare mortar may be exposed if the backing material tears, making it more difficult to resurface than when the transferred debonding material directly coats the mortar. This leads to the counterintuitive conclusion that adding a weak supplemental bond breaker layer (such as a textile or wax paper backing) may be detrimental because it blocks the protective transfer material from forming.

One-Way Sliding Test Results: Dynamic Breakaway Amplification

The one-way sliding tests were somewhat erratic owing to small deviations in the slip path and should be treated with a measure of caution. Nevertheless, the wear behavior and pressure dependency were similar, and the velocity dependency greater, than the two-way sliding tests. This was attributed to a recurring amplification at the start of each cycle, which was of similar magnitude as the first cycle of the two-way tests (Fig. 13). Neither the test rig inertial nor impact forces explain the amplification since these were also present during the two-way sliding reversals but found to be minimal. Instead, this appears to be a dynamic breakaway effect associated with transient viscoelastic hardening, which is also observed during shear tests (Kasai and Nishizawa 2010). The friction coefficient was +40% greater at the zero-displacement intercept for the $\delta_H = \pm 20$ mm tests, on average, but attenuated to the stabilized dynamic value with increasing slip distance. No amplification was observed at the zero-displacement intercept for the $\delta_H = \pm 40$ mm tests and only minimal amplification for the quasi-static tests.

Vertical Loading Test Results

The vertical load application at the start of each test series provided useful information as to the compressibility of the debonding materials, or effective debonding gap, which is important to accommodate Poisson expansion and controls the higher-mode buckling amplitude, thereby also contributing to the wavecrest friction force. It is important to note that the full debonding material thickness may not necessarily be easily compressed nor displaced, and the available thickness may be further reduced by permanent set induced by the hydrostatic pressure of the wet mortar.

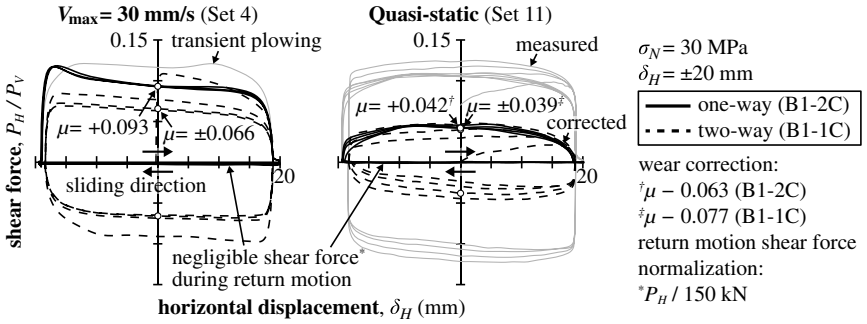

Fig. 13. Friction hysteresis, one-way sliding.

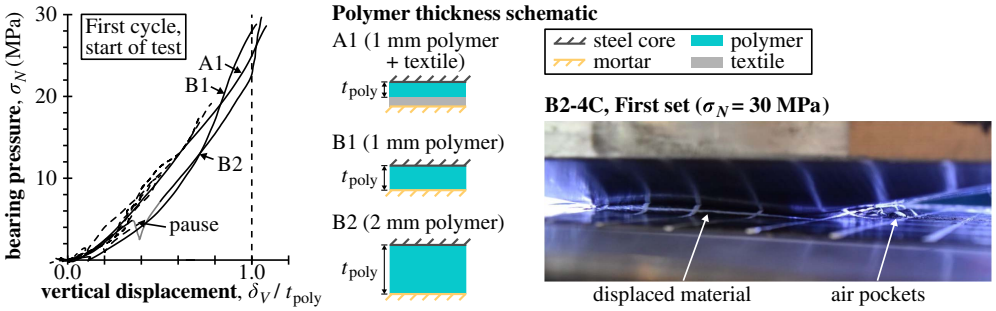

Fig. 14. Compression force-displacement of debonding material.

The vertical force-displacement plots are shown in Fig. 14 with the 30 MPa tests emphasized. The four vertical laser displacements were averaged and normalized by the polymer thickness (t_{poly}) measured prior to fabrication. Note that the vertical force starts from zero, because the 0.5 MPa precompression was removed to install the specimen. The debonding material was compressed by about 10% of the polymer thickness at $\sigma_N = 0.5$ MPa, then rapidly stiffened while undergoing plastic flow at higher pressures, with the displaced material forming permanent bulges on all four sides of the contact area, as well as some air pockets. Note that the open-sided test setup minimally confined the debonding material, such that it provides an upper bound of the debonding gap. Nevertheless, the vertical displacement nearly reached the polymer thickness by $\sigma_N = 25$ MPa, after which the mortar stiffness controlled. This produced a permanent clearance, with subsequent one-way sliding cycles displacing about 50% of the polymer thickness before registering a significant pressure. In design situations where a larger debonding gap is conservative, the polymer thickness may be directly adopted ($s_w = t_{poly}$), while textile backing should be excluded.

Analytical Friction Model

A nonlinear friction model was developed by calibrating and extending the pressure and velocity dependency equations from Kumar et al. (2015). The effective friction coefficient (μ) [Eq. (9)] was obtained from a reference value ($\mu_0 = 0.065$) taken at the third two-way sliding cycle with $\sigma_{N,0} = 20$ MPa and $V_{max,0} = 30$ mm/s and adjusted by dynamic breakaway (k_1), velocity (k_V), pressure (k_P), and wear (μ_W) modifiers. The k_1 modifier [Eq. (10)] accounts for the dynamic amplification observed at the start of each one-way sliding cycle (and first two-way sliding cycle) and decays from 1.8 to 1.0 over the first 40 mm of slip. The velocity modifier k_V [Eq. (11)] equals unity above $V_{max,0}$ and reduces to C_{slow} under quasi-static loading. The pressure modifier k_P [Eq. (12)] equals unity at $\sigma_{N,0}$, increases to C_{low} at zero pressure, and decreases to C_{high} at high pressures. Note that the product $k_1 k_V$ is constant under quasi-static conditions, and so these two terms should generally be considered together. Temperature dependency provides a small beneficial effect but was beyond the scope of this study, and so the compete model is given as

$$\mu = \mu_0 \cdot k_1 k_V \cdot k_P + \mu_W \tag{9}$$

$$k_1 = 1.8 - 0.02 \cdot |\delta_{slip}| \geq 1 \tag{10}$$

where $\mu_0 = 0.065$; and δ_{slip} = slip distance in current cycle (reset to zero whenever σ_N drops to zero) (mm)

$$k_V = 1 - (1 - C_{slow})\exp^{-r_V \cdot V_{slip}} \tag{11}$$

where V_{slip} = slip velocity (mm/s); $C_{slow} = 0.5$ (two-way), $0.6/k_1$ (one-way); and $r_V = 0.15$ s/mm

$$k_P = C_{high} - (C_{high} - C_{low})e^{-r_P \cdot \sigma_N} \tag{12}$$

where σ_N = bearing pressure [MPa]; $C_{high} = 0.85$; and $C_{low} = 2.5$; $r_P = (-1/\sigma_{N,0}) \ln[(C_{high} - 1)/(C_{high} - C_{low})] = 0.12$ MPa^{-1}.

The wear effect, which accounts for the partial exposure of the pressure- and velocity-insensitive mortar, is expressed by a wear coefficient μ_W [Eqs. (13*a*)–(13*c*)] integrated by the incremental slip ($d\delta_{slip}$). The wear coefficient is capped at $\mu_{W,max}$ owing to the self-healing resurfacing effect and only increases when the transient bearing pressure (σ_N) exceeds the wear initiating pressure ($\sigma_{N,W}$), which depends on the polymer thickness (t_{poly}) and varied from 10 to 25 MPa for the tested materials. Note that the reference initiating pressure ($\sigma_{N,W0}$), exponent (r_w), polymer thickness (t_{poly0}), and unit wear rate ($d\mu_{W0}$) may depend on the infill material, which included

25 MPa concrete and 50 MPa mortar in this study. However, only the mortar was tested above 30 MPa, and so it is recommended to set the wear coefficient to $\mu_{W,\max} = 0.15$ after exceeding the concrete strength

$$\sigma_{N,W} = \sigma_{N,W0} \cdot (1 - e^{-r_W(t_{\text{poly}} - t_{\text{poly0}})}) \geq 0 \tag{13a}$$

$$d\mu_W = d\mu_{W0}(\sigma_N - \sigma_{N,W}) \geq 0 \tag{13b}$$

$$\mu_W = \int_{\delta_{\text{slip}}} d\mu_W \cdot |d\delta_{\text{slip}}| \leq \mu_{W,\max} \tag{13c}$$

where t_{poly}: polymer thickness (mm); $d\delta_{\text{slip}}$ = incremental slip (m); σ_N: bearing pressure (MPa); $\sigma_{N,W0} = 25$ MPa; $r_W = 2.7$ mm^{-1}; $t_{\text{poly0}} = 0.4$ mm; $d\mu_{W0} = 6 \times 10^{-6}$ MPa^{-1}mm^{-1}; and $\mu_{W,\max} = 0.15$.

Fig. 15 compares the measured and predicted pressure, distance, and velocity dependencies, with the latter expressed by normalizing against the interpolated reference friction coefficients obtained at $V_{\max,0}$, which was repeated every third set. The pressure dependency increased sharply for $\sigma_N < 10$ MPa, but the load-control software prevented one-way sliding at these low bearing pressures, creating a data gap. The predicted wear dependency is in good agreement with the test results, even when the pressure varied from set to set and dominated for the thin A1 specimens and $\sigma_N > 30$ MPa. The one- and two-way friction coefficients converged for quasi-static and large-amplitude (±40 mm) sliding, while the velocity dependency peaked at $V_{\max} = 30$ mm/s, with higher velocities producing a beneficial cyclic heating effect, which is conservatively neglected.

Discussion

Friction Coefficient for Use in Numerical Simulation

The nonlinear friction model presented in Eqs. (9)–(13) was implemented as Abaqus/Explicit 2017 user subroutines (Sitler 2021). Given the complex dependencies and variable slip along the core yield length, simplified friction models indirectly calibrated against the BRB force-displacement hysteresis may be inaccurate when the core geometry or loading protocol significantly differs from the test specimen. Specifically, a larger friction coefficient is expected for thicker cores with smaller debonding gap ratios (s_w/t_c), as these produce lower bearing pressures, and for dynamic loading tests. Similarly, the greater cumulative slip displacement of longer cores increases the wear effect, which may be artificially suppressed in the small-scale specimens often used in academic studies.

Nevertheless, in some cases it may be reasonable to simplify the nonlinear friction model, specifically when the cumulative friction effects are small or to validate a complex model. In these cases, the small amplitude ($k_1 = 1.8$), high pressure ($\sigma_{N,0} = 30$ MPa, $k_P = 0.9$), slow speed ($V_{\max} < 5$ mm/s, $k_V = 0.7$), and final cycle ($\sum \delta_{\text{slip}} = 0.3$ m, $t_{\text{poly}} = 1$ mm, $\mu_W = 0.02$) friction coefficient of

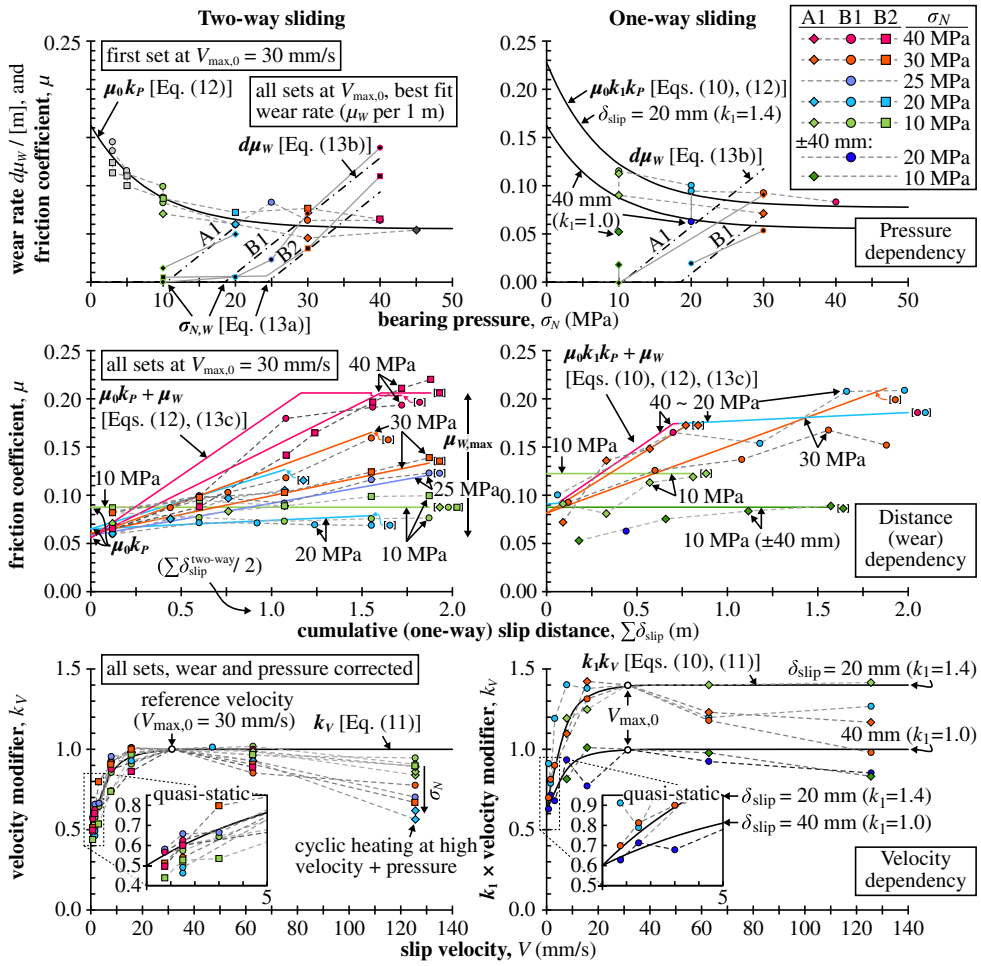

Fig. 15. Pressure, velocity, and distance (wear) dependencies.

$\mu = 0.09$ is nearly equal to the $\mu = 0.1$ used by many researchers and may be a reasonable starting point. However, in general, experimentally validated friction models that include the unique dynamic breakaway and wear effects are recommended, such as the proposed nonlinear friction model.

Quasi-Static Qualification Testing

Dynamic testing is not currently required by the AISC 341-16 specification owing to cost and test facility limitations (§Comm. K3.4, AISC 2016), while dynamic device-level tests have produced mixed results (Hasegawa et al. 1999; Lanning et al. 2016; Qu et al. 2020). However, the argument for incorporating loading rate effects fundamentally differs for the steel core, which is discussed in AISC 341-16, and the debonding material, which is not. Dynamic loading increases both the BRB forces and yield strengths of the force-controlled members, minimizing the change in the demand-to-capacity ratio. However, velocity-dependent friction exclusively affects demand, specifically by increasing the friction component (β_F) of the compressive adjustment factor (β).

This is an important distinction because the 2016 edition of AISC 341 §K3.8.d increased the acceptance criteria to $\beta < 1.5$, such that friction may now constitute up to approximately 40% of the quasi-static BRB compressive force, significantly increasing the potential influence of the friction coefficient on the overall behavior. Because dynamic testing introduces its own challenges, a practical approach may be to (1) obtain β from full-length quasi-static tests, (2) estimate the friction component as $\beta_F \approx \beta/(1 + 2\bar{\varepsilon})$, (3) scale the quasi-static β_F to an average dynamic value ($\beta_{F,dyn}$) using Eq. (14), and (4) recombine with the Poisson component to produce a design value of $\beta_{dyn} = \beta_{F,dyn} \times (1 + 2\bar{\varepsilon})$. This effectively reimposes the previous acceptance criteria of $\beta < 1.3$ for quasi-static tests, assuming $C_{\text{slow}} = 0.6/k_1 \approx 0.45$, while increasing the compression design forces by up to 20%. The unadjusted β test value may still be used for full-length dynamic testing, velocity-insensitive debonding materials (e.g., Interface type IV) or if friction is negligible (e.g., $\beta < 1.1$), otherwise, the following correction applies:

$$\beta_{F,dyn} = 1 + (\beta_F - 1) \cdot \int_0^{V_{\text{stroke}}} \frac{k_V(V)}{C_{\text{slow}}} \approx 1 + \frac{\beta_F - 1}{C_{\text{slow}}} \qquad (14)$$

Finally, dynamic tests with peak stroke velocities exceeding about 100 mm/s should produce similar friction velocity dependency due to the low saturation velocity of k_V. Cyclic heating may partially mitigate this adverse effect, but there are currently no comparative temperature data for full-scale BRBs, a prerequisite to take advantage of beneficial temperature dependency.

Conclusions

A novel friction experiment was conducted to evaluate the friction coefficient of soft, thin polymer BRB debonding interfaces at realistic bearing pressures, slip velocities, slip distances, and one-way sliding motion, where contact only occurs during the compression half-cycles:

- A preliminary numerical study indicated that the bearing pressure primarily depends on the debonding gap ratio (s_w/t_c) and varies from zero up to 50 MPa for typical applications.
- The slip velocity was almost equal to the relative core-mortar deformation rate (i.e., stroke velocity) at the core ends and then decreased nonlinearly to zero at the midspan shear key.
- Probabilistic single-cycle slip displacements were assessed as being 62% of the applied stroke displacement range ($2\delta_{\text{stroke}}$) and the cumulative slip distances as being 22% of the cumulative applied stoke, on average, with the latter rarely exceeding 2 m at fracture.
- The friction test of a bare steel-mortar control specimen produced a constant friction coefficient of $\mu = 0.75$, but this reduced to $\mu = 0.03$–0.25 for the debonded specimens.
- Two generally applicable, novel friction effects were identified. One-way sliding produced a recurring dynamic breakaway amplification that decayed with the single-cycle slip distance and was comparable to the first-cycle amplification observed for dynamic two-way sliding.
- Secondly, rapid wear of the soft polymers needed to accommodate Poisson expansion exposed small mortar patches, increasing the friction coefficient with the cumulative slip distance.
- A nonlinear pressure–velocity–displacement–dependent friction model was proposed, significantly improving upon the Coulomb friction estimates used in current practice.

Data Availability Statement

Some or all data, models, or code that support the findings of this study are available from the corresponding author upon reasonable request (experimental results and postprocessing code).

Acknowledgments

The authors thank Nippon Steel Engineering for providing the test specimens, and specifically Mr. Kenichi Hayashi for managing the specimen fabrication.

References

AISC. 2016. *Seismic provisions for structural steel buildings*. AISC 341-16. Chicago: AISC.

Avci-Karatas, C., O. C. Celik, and S. Ozmen Eruslu. 2019. "Modeling of buckling restrained braces (BRBs) using full-scale experimental data." *KSCE J. Civ. Eng.* 23 (10): 4431–4444. https://doi.org/10.1007/s12205-019-2430-y.

Black, C. J., N. Makris, and I. D. Aiken. 2004. "Component testing, seismic evaluation and characterization of buckling-restrained braces." *J. Struct. Eng.* 130 (6): 880–894. https://doi.org/10.1061/(ASCE)0733-9445(2004)130:6(880).

Budaházy, V., and L. Dunai. 2015. "Numerical analysis of concrete filled buckling restrained braces." *J. Constr. Steel Res.* 115 (Dec): 92–105. https://doi.org/10.1016/j.jcsr.2015.07.028.

Chen, Q., C. L. Wang, S. Meng, and B. Zeng. 2016. "Effect of the unbonding materials on the mechanic behavior of all-steel buckling-restrained braces." *Eng. Struct.* 111 (Mar): 478–493. https://doi.org/10.1016/j.engstruct.2015.12.030.

Guo, Y. L., J. Z. Tong, X. A. Wang, and B. H. Zhang. 2017. "Subassemblage tests and numerical analyses of buckling-restrained braces under pre-compression." *Eng. Struct.* 138 (May): 473–489. https://doi.org/10.1016/j.engstruct.2017.02.046.

Hasegawa, H., T. Takeuchi, M. Iwata, S. Yamada, and H. Akiyama. 1999. "Experimental study on dynamic behavior of unbonded braces." [in Japanese] *AIJ J. Tech. Des.* 5 (9): 103–106. https://doi.org/10.3130/aijt.5.103.

Iwata, M., T. Kato, and A. Wada. 2000. "Buckling-restrained braces as hysteretic dampers." In *Behaviour of steel structures in seismic areas*, 33–38. Boca Raton, FL: CRC Press.

Kasai, K., and K. Nishizawa. 2010. "Experiments and dynamic analysis method for buckling restrained brace." [in Japanese] In *Proc., AIJ Annual Meeting*, 807–808. Toyama, Japan: Architectural Institute of Japan. https://www.aij.or.jp/paper/detail.html?productId=221821.

Kumar, M., A. S. Whittaker, and M. C. Constantinou. 2015. "Characterizing friction in sliding isolation bearings." *Earthquake Eng. Struct. Dyn.* 44 (9): 1409–1425. https://doi.org/10.1002/eqe.2524.

Lanning, J., G. Benzoni, and C. M. Uang. 2016. "Using buckling-restrained braces on long-span bridges. I: Full-scale testing and design implications." *J. Bridge Eng.* 21 (5): 04016001. https://doi.org/10.1061/(ASCE)BE.1943-5592.0000781.

Qu, Z., X. Jinzhen, Y. Cao, W. Li, and T. Wang. 2020. "Effects of strain rate on the hysteretic behavior of buckling-restrained braces." *J. Struct. Eng.* 146 (1): 06019003. https://doi.org/10.1061/(ASCE)ST.1943-541X.0002486.

Sitler, B. 2021. "Development of a multistage buckling-restrained brace and higher-mode buckling friction model for long cores." Ph.D. thesis, Dept. of Architecture and Building Engineering, Tokyo Institute of Technology.

Sitler, B., and T. Takeuchi. 2021. "Higher-mode buckling and friction in long and large-scale buckling-restrained braces." *Struct. Des. Tall Spec. Build.* 30 (1): e1812. https://doi.org/10.1002/tal.1812.

Smith, M. 2017. *ABAQUS/explicit user's manual, version 2017*. Providence, RI: Simulia.

Stachowiak, G., and A. Batchelor. 2014. *Engineering tribology*. Amsterdam, Netherlands: Butterworth-Heinemann.

Stratan, A., C. I. Zub, and D. Dubina. 2020. "Prequalification of a set of buckling restrained braces: Part II—Numerical simulations." *Steel Compos. Struct.* 34 (4): 561–580. https://doi.org/10.12989/scs.2020.34.4.561.

Tsai, K. C., A. C. Wu, C. Y. Wei, P. C. Lin, M. C. Chuang, and Y. J. Yu. 2014. "Welded end-slot connections and debonding layers for BRBs." *Earthquake Eng. Struct. Dyn.* 43 (12): 1785–1807. https://doi.org/10.1002/eqe.2423.

Yoshikawa, H., K. Nishimoto, H. Konishi, and A. Watanabe. 2010. "*Fatigue properties of unbonded braces and u-shaped steel dampers.*" [in Japanese] Nippon Steel Engineering Technical Report. Tokyo: Nippon Steel.